Reaction Chemistry & Engineering

Linking fundamental chemistry and engineering to create scalable, efficient processes

Accepted Manuscript

This article can be cited before page numbers have been issued, to do this please use: J. Bárta, L. Procházková, M. Škodová, K. Dcká, X. Popovi, T. J. Pavelková, P. Beck and V. uba, *React. Chem. Eng.*, 2022, DOI: 10.1039/D1RE00374G.

ROYAL SOCIETY OF CHEMISTRY

rsc.li/reaction-engineering

DOI: 10.1039/D1RE00374G

Advanced photochemical processes for the manufacture of nanopowders: an evaluation of long-term pilot plant operation

Jan Bárta[a], Lenka Prouzová Procházková[a,b], Michaela Škodová[a], Kateřina Děcká[a], Kseniya Popovich[a], Tereza Janoušková Pavelková[a], Patrik Beck[c] and Václav Čuba [a,*]

a Department of Nuclear Chemistry, Faculty of Nuclear Sciences and Physical Engineering, Czech Technical University in Prague, Břehová 7, 115 19 Prague 1, Czech Republic

b Institute of Physics, Czech Academy of Sciences, Cukrovarnická 10, 162 00 Prague 6, Czech Republic

c Tesla V.T. Mikroel, Nademlejnská 600/1, 198 00 Prague 9, Czech Republic

** corresponding author: vaclav.cuba@fjfi.cvut.cz*

Abstract

In this study, an UV light-based technology for syntheses of nano-dimensional metal oxides feasible in industrial scale is proposed, based on our long term experience with the operation of a photochemical pilot plant. We demonstrate the synthesis, properties and manufacturing costs with a case study for ZnO, $Y_3Al_5O_{12}$ and $Gd_3Ga_2Al_3O_{12}$ materials that are comparable with the laboratory-scale yields and purity. The process relies on irradiation of aqueous solutions containing dissolved precursors, typically formate anions and soluble metal salts, by 254 nm UV light. Depending on the solution composition, UV irradiation leads to the formation of nanocrystalline or amorphous product of particulate or gel-like character. This material can be either used as is, or further processed, usually by drying in air and heat-treating at elevated temperatures (200–1200 °C), leading to a fine powder suitable for a subsequent use in different applications. A number of syntheses were made during the past years to provide an evaluation of various aspects influencing the manufacturing process such as solution composition or character of the product. The observed yields were correlated with both the concentration of the salts in solutions and the irradiation time; then, photochemical production rates were determined, and the potential of this method for up-scaling was evaluated. X-ray diffraction results and radioluminescence measurements evidence that the phase purity and emission spectra of the produced materials are fully comparable to laboratory-scale preparations. Realistic assumptions and considerations were then used for a comprehensive estimation of manufacturing costs in the described photochemical pilot plant and the parameters leading to lower manufacturing costs were identified.

View Article Online
DOI: 10.1039/D1RE00374G

1 Introduction

Nanopowders, nanogels and colloid solutions containing either pure compounds, composite nanoparticles or particles with controlled amounts of various dopants have a wide range of applications, including sorbents, catalysts, electrooptical materials, precursors of scintillating materials for industrial (scintillating ceramics) or medicinal applications such as in photodynamic therapy (PDT) [1–5].

Despite the rapid development of nanotechnologies in recent decades, a large-scale cost-effective manufacture of pure and fine nanopowders in sufficient volumes still remains a challenge, even though an extensive range of new applications for these materials in the industry or (bio)medicine emerged more than a decade ago[1] and there is a substantial demand for suitable nanomaterials. The requirements for chemical and/or phase purity of synthesized materials in various fields of industry are stringent; therefore, one of the main tasks for the researchers in nanotechnology is to reduce the complexity and increase the efficiency of the purification process. Production of nanomaterials, though, accentuates immediate use of prepared materials without additional purification procedures. In addition, the whole manufacturing process should be as cost-effective and feasible as possible, which requires minimizing both the number of operational steps and the manpower required.

One of the promising preparative techniques relies on chemical reactions initiated and maintained by the absorption of ionizing or non-ionizing radiation; radiation-induced preparative methods utilizing high-energy ionizing radiation has proven their capability for synthesis of a broad range of nanocrystalline materials, as was reported for various oxides elsewhere [6–14]. They have several advantages, such as independence on the experimental conditions, low activation energy, high yields and high reaction rates. However, operating a source of ionizing radiation is required, which also increases requirements for qualified personnel and the cost of the process, including substantial capital costs.

In contrast, one of the main advantages of UV-light-based reactions is their ease of use in a standard chemical laboratory and that the process does not require radiation-qualified personnel to be carried out. Moreover, chemical yields in case of UV-light reaction route can be very high (often above 95%) and production rate of UV-light-induced synthesis is also comparable with ionizing radiation-induced process on a similar scale. In fact, UV irradiation route may lead to better products than ionizing radiation, such as in the case of yttrium aluminum garnet $Y_3Al_5O_{12}$; phase-pure garnet was obtained using UV or gamma-ray

irradiation [11,13], while electron beam irradiation caused the appearance of impurities like Y_2O_3 [11]. In both types of radiation synthesis, the process does not rely on thermal reactions and generally stops when the irradiation is terminated, giving a great degree of control over the process.

The principle of UV-light-induced methods of preparation is based on reactions of dissolved precursors (usually metal salts) with highly reactive intermediates formed by photolysis of either water molecules, or various photo-active additives excited by visible or UV light (photosensitizers) – for further details on the reactions mentioned below, see ref. 15,16 and the references therein. In general, the irradiation generates reactive radicals or ion-radicals that quickly react with the surrounding medium or chemicals dissolved in it at rate constants of $k \sim 10^6$ to 10^{10} dm^3 mol^{-1} s^{-1}; the reactions detailed below are well established and proven by many pulse radiolysis or flash photolysis studies. The water photolysis proceeds according to the following equation [17–19]:

$$H_2O \overset{h\nu}{\rightarrow}{}^{*} \cdot OH + \cdot H$$

Radical scavengers play a very important role in this process. A typical example is a formate ion $HCOO^-$ that transforms into $\cdot COO^-$ ion-radical, a strong reducing agent widely used in radiation chemistry:

$$\cdot COO^- + Me^{n+} \rightarrow Me^{(n-1)+} + CO_2$$

This radical can be formed by direct photolysis of formate anion (thus, formate is also a photosensitizer [20]):

$$HCOO^- \overset{h\nu}{\rightarrow} \cdot H + \cdot COO^-$$

Other reaction channels of formate ion may lead to the formation of hydrated electrons and ·OH radicals:

$$HCOO^- \overset{h\nu}{\rightarrow} H\dot{C}OO + e_{aq}^-$$

$$HCOO^- \overset{h\nu}{\rightarrow} H\dot{C}O + \cdot O^- \leftrightarrow \cdot OH$$

The $\cdot COO^-$ ion-radical also reacts with oxygen dissolved in aqueous solutions, producing carbon dioxide and (hydrogen) carbonates:

$$\cdot COO^- + O_2 \rightarrow \cdot O_2^- + CO_2 \leftrightarrow H\dot{O}_2, CO_3^{2-}, HCO_3^-$$

The overall diagram of the process is shown in Fig. 1 with all main reactions involved. However, some of the reactions involved in the photochemical synthesis of oxide (nano)materials are still not completely understood and require further investigation.

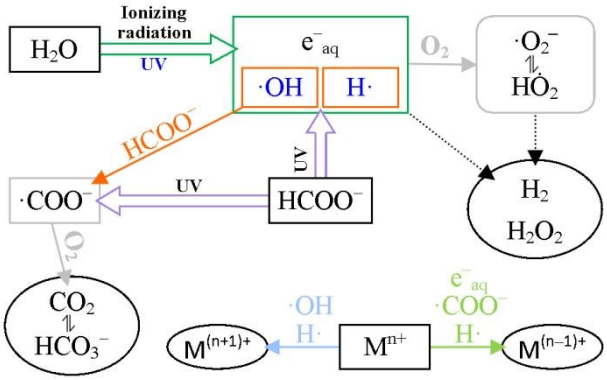

Figure 1 – Diagram of processes involved in radiolysis and photolysis of aqueous solutions

Nowadays, photoreactions in industrial scale encompass e.g. photo-induced polymerizations, waste water treatment and ultraviolet germicidal irradiation as a disinfection method. Photo-induced syntheses are also used for preparation of miscellaneous materials in photoreactors [21,22], while photo-catalytic processes are used e.g. in self-cleaning surfaces or chemical conversions [23–25]. However, large scale photochemical production of nanosized materials remains largely unexplored, although laboratory scale syntheses of various nanocrystalline materials, such as synthetic garnets [11,26], ZnO [27,28], Y_2O_3 [29], CeO_2 [14] and other compounds have been already reported. In the case of CeO_2, its application potential for degradation of organophosphorous compounds as well as manufacturing costs were evaluated for various synthesis methods, including direct photochemical synthesis in large scale [30].

In this study, we describe a facile, rapid and effective photochemical method, prospective for producing nanocrystalline materials from aqueous solutions in industrial scale. We also evaluate a long term operational experience running a demonstration pilot plant for photochemical syntheses of nanocrystalline materials that incorporates the readily available and cost-efficient low-pressure mercury discharges as the irradiation source. Furthermore, the evaluation of factors influencing UV-light induced production rate of desired materials or their solid precursors is given. Additionally, the manufacturing costs of materials using the described pilot plant are estimated in a great detail, the most important contributions to it are thoroughly assessed, and possible solutions aimed at lowering the overall costs are suggested.

Our long-term experience with operating a photochemical pilot plant was focused mainly on the synthesis of following nanocrystalline materials: zinc oxide doped with gallium (ZnO:Ga), yttrium-aluminium garnet doped with cerium $Y_3Al_5O_{12}$:Ce (YAG:Ce) and gadolinium-gallium-aluminium garnet doped with cerium $Gd_3(Ga,Al)_5O_{12}$:Ce (GGAG:Ce). All these materials were selected for their importance / prospectiveness in industrial applications.

The first abovementioned material, ZnO:Ga, can be processed into an ultrafast scintillator with intense excitonic luminescence in the UV region (390 nm) and sub-nanosecond scintillation decay time [28], which is especially atractive for applications in high-energy physics and positron emission tomography with time-of-flight detection (TOF-PET). In our earlier study, it was found that photo-induced synthesis of nanopowder precursor ZnO_2:Ga and its further heat treatment led to the formation of scintillation particles with appropriate properties [28]. An important component for the synthesis of this zinc peroxide is hydrogen peroxide H_2O_2 that efficiently absorbs UV photons and splits into ·OH radicals; however, the exact mechanism of the photochemical synthesis of ZnO_2 is unknown and only the overall reaction equations can be found in the literature [31]. By varying the reaction conditions, compounds like basic carbonates $Zn_x(CO_3)_y(OH)_z$ and basic nitrates $Zn_x(NO_3)_y(OH)_z$ can be synthesized by photochemical methods as well – these compounds then endothermically transform into ZnO upon mild heating.

The remaining two materials investigated are cubic oxide luminophores with a garnet structure (derived from pyrope, "Bohemian garnet") with general formula of $A_3B_2C_3O_{12}$ (A = rare earth metals Y, La-Lu; B/C = Al, Ga). These synthetical materials possess a broad band gap (i.e. they are insulating, colour-less materials) and have a great potential in many applications determined mainly by the dopant used – typically, optically active lanthanide ions. Thus, e.g. single-crystalline YAG:Nd^{3+} is one of the most widely used materials in IR lasers [32], whereas Ce^{3+} as a dopant causes relatively fast and bright green luminescence utilized in scintillating detectors of radiation or white LEDs [33]. Due to a more complex crystal structure and high melting point, formation of garnets usually requires rather high temperatures, at least 900 °C for photochemically or sol-gel synthesized precursors [26,32] and above ~ 1500 °C in the case of solid state reactions [34].

2 Experimental

All chemicals used in this work were purchased from Merck, Carl Roth or Penta, and used as received (purity > 98%). Aqueous solutions of rare earth nitrates were prepared by dissolving the corresponding oxides (Merck) in stoichiometric amount of hot diluted nitric acid (Penta). A similar approach was used with dissolution of β-Ga_2O_3 (Merck); it was found that 100% excess of hot diluted hydrochloric acid (Penta) is needed to fully dissolve it. To suppress the excessive acidity after complete dissolution of Ga_2O_3, either ammonia (Penta) was used, or the surplus amount of acid was utilized to dissolve the rare-earth oxides in this

solution. Soluble aluminium or zinc salts (Merck) and ammonium formate (Carl Roth) were directly dissolved in the solutions. In the photochemical synthesis of ZnO_2 and hydrozincite, 30 % hydrogen peroxide solution (Penta) was also used to set H_2O_2 concentration in the initial solutions between 0.1 and 1 mol dm^{-3}.

The UV-light-induced syntheses were carried out in our photochemical pilot plant, a utility-model-protected double-walled reactor prototype (Fig. 2); its normal operation procedure is described below. The reaction mixture is loaded in the reactor using a peristaltic pump (Fig. 2h), the liquid in the photoreactor vessel (Fig. 2a) is then continually stirred by an anchor stirrer (Fig. 2d) and circulated through a sedimentation tank (Fig. 2e) that partially separates the product from the circulating solution. The photoreactor consists of 28 submersible low-pressure mercury discharges (UV lamps, T5Q408-4P-44W; power input à 44 W, light output à ~ 12 W, λ_{UV} = 253.6 nm) with fused silica tube as an outer layer (Fig. 2c). Their emission wavelength coincides with the absorption spectra of both formates and nitrates [26] as well as hydrogen peroxide [27], ensuring reasonably efficient photochemical reactions. The space between the two walls of the reactor vessel enables cooling of the reaction mixture by a 2 kW water chiller unit (cooling power 1.18 kW, Fig. 2g). When the synthesis is finished, the product is collected from the sedimentation tank (Fig. 2e). During the irradiation, samples of the circulating solution were taken and analyzed. Their pH value was determined with a Jenway 3540 pH-meter with glass electrode. The chemical yield can also be easily observed during the irradiation process by addition of precipitant (e.g. sodium hydrogen carbonate or potassium oxalate) to the centrifuged liquid samples.

The solid precursors (gelatinous solid phase or fine powder) were separated from the irradiated solution using decantation and either centrifugation (MPW 350 centrifuge) or microfiltration (Amicon cell with 500 mL internal volume; Millipore HAWP membrane filter, 0.45 μm), dried at 40 °C and heat treated to decompose into oxides (final product) using Clasic 0415 VAC vacuum chamber furnace. The total synthesis yield, which is lower than the chemical yield due to separation losses, was calculated from the weight of final calcined oxide. In a few cases, the synthesized gelatinous product was used directly for further processing, in which case the synthesis yield could not be determined precisely.

Phase purity of products was characterized by X-ray powder diffraction (XRPD) using Rigaku MiniFlex 600 diffractometer equipped with Cu X-ray tube and NaI:Tl scintillation detector. The measured diffraction patterns were then compared to the powder diffraction records from the ICDD structural database PDF-2 (version 2013). The crystallite size *l* [nm] was determined from the integral width of all diffraction lines

using weighted linear regression and Halder-Wagner linearization based on the parabolic approximation of true Voigt profile width:

$$\frac{\beta^2_{\text{sample},i}}{\tan^2\theta_i} = \frac{K \cdot \lambda}{l} \cdot \frac{\beta_{\text{sample},\,i}}{\tan\theta_i \cdot \sin\theta_i} + \varepsilon^2, \quad (1)$$

where $\beta_{\text{sample},i}$ [rad] is the integral width of a peak at diffraction angle $2\theta_i$ that has the instrumental broadening contribution subtracted from it, ε is the microstructural strain, K is a Scherrer constant and λ is the X-ray beam wavelength (Cu-K_α, 0.154184 nm).

The elemental composition of solid precursors was determined by X-ray fluorescence analysis (XRF) using Niton XL3t 900S GOLDD analyzer (Ag anode) in the Cu/Zn Mining mode. Luminescence properties were evaluated by measuring photoluminescence (PL) and radioluminescence emission spectra (RL) using the custom-made spectrofluorometer 5000M (Horiba Jobin Yvon), equipped with X-ray source DEBYFLEX ID3003 (Seifert Gmbh) with a DX-W 10x1-S 2400 W tube (tungsten anode).

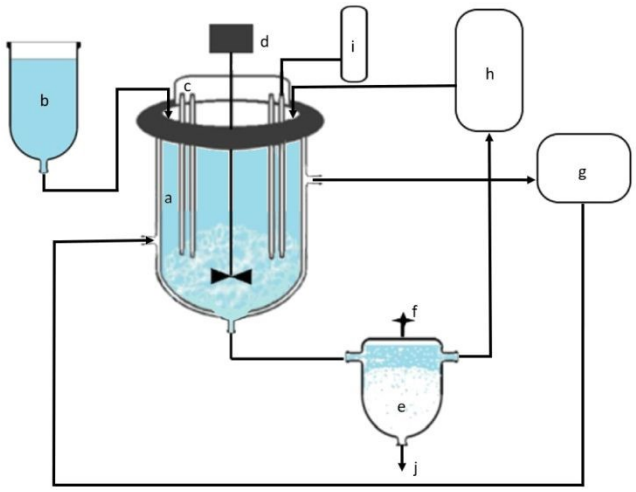

Figure 2 – Photochemical pilot plant; a – double-walled photoreactor vessel, b – water/acid dosing tank, c – lid with submersible UV lamps, d – anchor stirrer, e – sedimentation tank, f – vent valve, g – recirculating cooler; h – peristaltic pump, i – UV lamps' power source, j – product drain

3 Results and Discussion

3.1 Preparation process

The pilot plant described above has proven to be suited for a long-term, largely unmanned operation. Due to a monitoring and remote controls installed, only the loading of the reactor, initial startup, draining of the irradiated liquid as well as product separation require human overview. Total synthesis yields of prepared garnet nanocrystalline materials in batch experiments generally reach around 90-95 %, as shown in Table 1

and Fig. 3, provided that adequate irradiation time is used; a more detailed overview is shown in the Supplementary Information file. The precipitation of solid precursors for garnets with a molar ratio of metal ions to formate M^{3+}:$HCOO^-$ = 8:100 has been observed to have a moderate threshold irradiation time, after which the product precipitation from a previously clear aqueous solution starts to occur. This "lag phase" applies for most systems under study and the start of precipitation is easily observable by a slight turbidity of the solution. For a given solution volume and UV light power used, this threshold irradiation time increases with solution concentration, as can be seen from the changes in the approximate concentration of free rare earth ions in Fig. 3. In the case of zinc oxide synthesized through the peroxide route (ZnO_2 [27,28]), the total synthesis yields in batch experiments in the pilot plant were much lower than the expected chemical yields, reaching only about 36 %. This was mainly caused by losses of the product due to its observed sorption on all surfaces, including photoreactor walls and protective tubes of the UV lamps. At H_2O_2 concentrations ≤ 0.5 mol dm^{-3}, the sorption of the product significantly reduced and yield increased (see Table 1), but the product composition changed from ZnO_2 to a hydrozincite phase $Zn_5(OH)_6(CO_3)_2$ (see below); a minor nanocrystalline ZnO_2 presence cannot be excluded.

The difficulty of product separation out of the residual solution depends on its form; for powder-like solids (ZnO_2, garnet precursors from solutions with higher initial concentrations of salts), classical vacuum filtration through a HAWP membrane proved to be sufficient and fast enough. Gelatinous products like garnet precursors from relatively diluted solutions (≤ 2×10^{-3} mol dm^{-3} of garnet) tend to clog filters very fast and can be separated either by a lengthy centrifugation, or using a pressurized microfiltration unit with a generally small inner volume. Both procedures require almost constant human overview, but a large-volume custom-made microfiltration unit has been recently built at Tesla V.T. Mikroel by Kavalierglass that significantly lowers the time required. The thick gel produced by centrifugation or microfiltration (the latter with a rather low amount of constituent liquid) is then dried to solid chunks – collapsed xerogel; residual salts from the liquid are fully decomposed during subsequent calcination.

Table 1 lists the materials synthesized using the photochemical pilot plant, their compositions (or ranges of concentrations), achieved synthesis yields and the weight of the obtained product divided by the total radiant energy of the UV light used in its synthesis [megajoules, MJ], which we designated as a photochemical production rate. To calculate this value, declared light power output of the UV discharges (28 lamps à 12 W, 336 W in total) was multiplied by the irradiation time used.

We presume that post irradiation, the aqueous solutions with remaining unspent precursors can be still used for a new production run, i.e. fresh precursors can be added to replace the spent part, which contributes to the cost effectiveness of the process. In that case, care must be taken to select salts that would not be concentrated in the solution during the subsequent runs. To elaborate further, the nitrates NO_3^- added as counter-ions to e.g. Al^{3+} may be partially reduced during irradiation into nitrites NO_2^-, but the remaining nitrates will not be incorporated in the formed solid phase in any great quantities. Even for a hydrozincite-related $Zn_5(OH)_8(NO_3)_2$ phase, only ~ 20% of initial nitrates may be expected in the synthesized solid product and the rest will remain in the solution. Thus, if more metal nitrate salts are added for the second run, the total NO_3^- concentration increases significantly. Similar situation is going to occur for surplus HCO_3^-, formed in the photochemical process, and for ammonia NH_4^+. Therefore, for truly continuous photochemical preparation with the highest possible production rate, the concentrations of the main intermediates would need to be observed and controlled so as to prevent their excessive build-up.

Table 1 – Compositions, synthesis yields and photochemical production rates (weight of synthesized product per radiant energy of UV light) of various compounds synthesized in the photochemical pilot plant.

Compound	Initial solution composition	Synthesis yield	Photochemical production rate [g / MJ_{UV}]
$Y_3Al_5O_{12}$ (YAG)	$3x$ M† Y^{3+} nitrate, $5x$ M Al^{3+} nitrate, $100x$ M $HCOONH_4$	93–95 %	~ 3.5
$Gd_3Ga_2Al_3O_{12}$ (GGAG)	$3x$ M Gd^{3+} nitrate, $2x$ M Ga^{3+} nitrate, $3x$ M Al^{3+} nitrate, $100x$ M $HCOONH_4$	93 %	~ 4.5
ZnO_2	y M‡ Zn^{2+} nitrate, $2y$ M $HCOONH_4$, 1.00 M H_2O_2	29–36 %	1.5–4.0
$Zn_5(OH)_6(CO_3)_2$	y M Zn^{2+} nitrate, $2y$ M $HCOONH_4$, 0.20–0.50 M H_2O_2	45–84 %	3.8–45

† x = garnet solution concentration (5×10^{-4} – 8×10^{-3} mol dm^{-3}); M = mol dm^{-3}

‡ y = zinc concentration (0.01 – 0.05 mol dm^{-3})

The initial pH of the solutions, typically in the 4.5-6.5 range, is determined mainly by the presence of dissolved metal salts and the presence of formate ion serving as ·OH radicals scavenger and the photoactive compound. Slightly acidic initial pH reflects the fact that all metal ions used are moderate to weak bases, whereas nitric acid (nitrates) is a very strong acid. During the irradiation, the pH value gradually changes, as shown in Fig. 3. Obviously, the nature of the change strongly depends on the solution composition. The main contribution comes from a gradual decomposition of the ammonium formate present in the solution to NH_3 and CO_2 (forming carbonates); both H_2CO_3 and HCO_3^- are much weaker acids than the original HCOOH and

thus the pH increases. In the case of garnet synthesis, formation of the gelatinous solid phase started above pH ~ 5.5; this may be connected to the observed threshold time in product formation (precipitation of amorphous mixed carbonates, basic carbonates or hydroxides). In the case of ZnO_2, the increase in pH caused by formate decomposition is most likely not related to product formation, which is observed from the very beginning of irradiation.

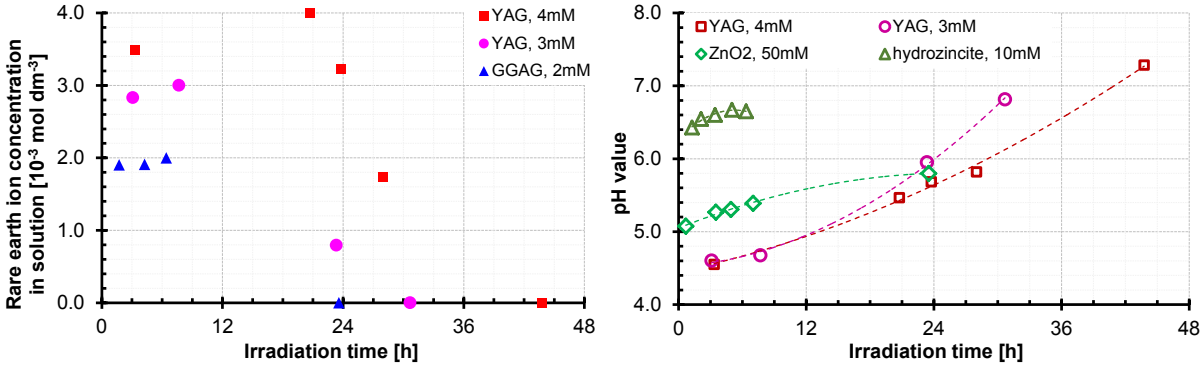

Figure 3 – Left: changes in concentration of residual rare earth ions with irradiation time (YAG, GGAG), estimated from the amount of oxalate precipitate obtained; Right: changes in pH during the irradiation (YAG, ZnO_2, $Zn_5(OH)_6(CO_3)_2$), dashed lines are guide for the eye. Error bars for the experimental uncertainties are smaller than the data points.

Photochemical synthesis can be readily upscaled. Based on the results of several runs with different initial concentration of solutions, it seems that the garnet preparation process is additive, and the irradiation time necessary to obtain maximum yield increases roughly linearly with the initial concentration, as shown in Fig 4. The irradiation time necessary for near-quantitative preparation determined by the absence of rare earth metals in the solutions (see Fig. 3) is shown on the y-axis as solid diamonds. Insufficient irradiation time (below the dashed line for a given initial concentration) leads to lower synthesis yields, as indicated by the empty square data points. Thanks to a similar chemistry of all rare earth ions, no difference was observed between garnets with different composition (e.g. YAG or GGAG) regarding the required irradiation time. This apparently linear relation together with rather high yields makes the photochemical preparations of garnets a good candidate for industrial upscaling. Garnets with heavier elements (e.g. GGAG) will naturally have, due to their larger molar mass, an apparently higher production rate (see Table 1).

Similar proportional scaling of solution composition in the synthesis of ZnO did not result in a comparable linear behaviour, as the product composition changed from ZnO_2 (50 mmol dm^{-3} Zn^{2+} + 1 mol dm^{-3} H_2O_2) to hydrozincite $Zn_5(OH)_6(CO_3)_2$ (10 mmol dm^{-3} Zn^{2+} + 0.2 mol dm^{-3} H_2O_2) – see Fig. 5. The main influence on

DOI: 10.1039/D1RE00374G

the product composition and the photochemical process seems to be the absolute concentration of hydrogen peroxide, not its ratio to the concentration of Zn^{2+}.

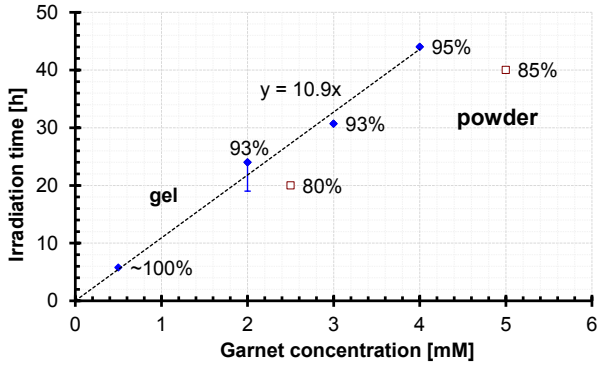

Figure 4 – Dependence of irradiation time required for near-quantitative garnet synthesis on the initial precursor concentration (numbers beside data points indicate the total synthesis yield achieved) for 28×44W mercury lamps irradiating 80 L solution.

3.2 Product characterization

The phase purity of produced materials is generally excellent when the solutions have proper composition (e.g. stoichiometry), as shown in Fig. 5. Although the X-ray diffraction is known to have moderate limits of detection (~ 1 % depending on the materials within the sample), an XRD pattern provides a phase purity assessment that is more than sufficient for industrial synthesis of inorganic materials. Dried xerogel of the solid precursors for garnets (amorphous carbonate-containing solid) starts to crystallize into a cubic garnet lattice at ~ 900 °C [11,26]; however, calcination of large amounts of these precursors in a static atmosphere can result into a minor "hexagonal $YAlO_3$"-type impurity ($Y_3Al_3O_8CO_3$) as well [32,35]. Calcination in thin layers, flowing atmosphere or above 1100 °C leads to phase-pure samples; in addition, short annealing at ~ 1200 °C is often required to achieve the best luminescent properties of garnets in their use as luminescent materials. Similarly, ZnO_2 and $Zn_5(OH)_6(CO_3)_2$ also require additional heat treatment to achieve the desired composition / properties of ZnO.

As with any other preparation method, the size of the particles depends strongly on the type of post-irradiation processing (if any) and the material itself. On the other hand, their size distribution tends to be rather narrow in radiation syntheses – the UV radiation penetrates the whole irradiated volume and causes a homogeneous precipitation of gel or simultaneous formation of nuclei. However, a clear distinction must be made between physical particle size, their hydrodynamic diameter (DLS) and crystallite size (XRPD) – the

filtration involved in the product separation and subsequent required calcination processes cause significant intergrowth of particles; for basic process optimization of crystalline materials, the most convenient size determination is the crystallite size. The moderate width of diffraction peaks in Fig. 5 evidences that even after calcination at 1200 °C for 2 hours, the YAG phase retained a rather small crystallite size of ~ 43(4) nm, while the short calcination at 1000 °C produced nanocrystalline powder with a crystallite size of ~ 18(1) nm. In the case of ZnO_2, the synthesized material with very broad diffraction peaks (very small crystallite size) violently decomposed at 200 °C to crystalline hexagonal ZnO with a very small crystallite size of ~ 6(2) nm (see Fig. 5). Therefore, given proper separation and heat treatment procedures, this method allows a reasonably fast production of nanomaterials with large yields.

One of the biggest advantages of this method is that the reaction is initiated by the absorption of radiant energy and controlled by the total amount of light absorbed and photon flux. There are no additives, catalysts or other chemicals added to the solutions aside from the metal salts of the product constituents and a scavenger / photosensitizer. This translates into naturally high purity of prepared materials. On the other hand, this method is also applicable to a very broad range of metal elements, so most metal ions present in the solutions can be easily and quantitatively incorporated in the formed solid phase, requiring rather pure initial compounds (see radioluminescence spectra below). The use of very pure metal salts results in no chemical impurities detectable by X-ray fluorescence analysis. This method is, with some exceptions, essentially a homogeneous precipitation, so all the metal ions are distributed almost homogeneously in the solid phase, requiring only a short calcination at rather low temperatures to achieve phase-pure multi-component oxides. Compared to energy-consuming solid state reactions requiring long heat treatments at high temperatures, this offers a significant cost reduction. As another result of this homogeneity, no phase impurities are typically observed in XRD patterns (within the limit of detection of XRD).

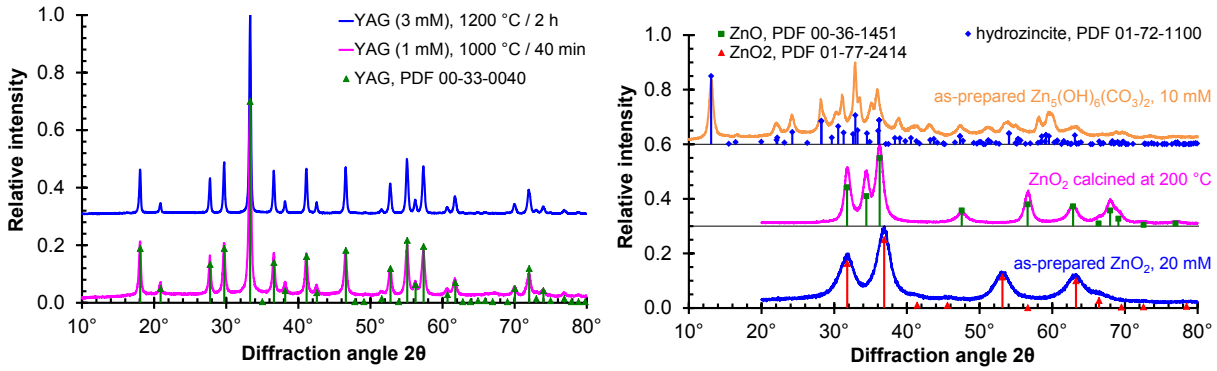

Figure 5 – Typical XRD patterns of prepared materials (left – YAG, right – ZnO) compared to ICDD PDF-2 records of the corresponding phases.

The application potential of the garnet materials as suitable hosts for luminescent ions is illustrated by radioluminescence spectra of Ce-doped YAG in Fig. 6 and their comparison to powdered $Bi_4Ge_3O_{12}$ reference scintillator (BGO). The spectra in Fig. 6 feature a very intense parity-allowed Ce^{3+} $5d-4f$ emission in the green region (~ 520 nm) [11,26], a very weak defect emission in the near UV and several impurity-related emission features: Cr^{3+} R-line doublet and its associated phonon lines around 700 nm, small Gd^{3+} $4f-4f$ emission at ~ 310 nm and an onset of Fe^{3+} emission from garnets at > 750 nm. All observed trace impurities are quite commonly found in synthetic garnets; because of their chemical similarity to the materials used (Fe and Cr ~ Al; Gd ~ Y), they can be attributed to impurities present in the initial metal salts. The presence of Gd can also be a result of incomplete washing of the system after a previous GGAG synthesis; therefore, high purity chemicals and thorough washing of the system by diluted nitric acid are necessary steps for achieving the best materials possible. Despite the trace impurities, the synthesized YAG:Ce is still a very bright luminophore (evident from its radioluminescence intensity well surpassing that of the BGO), which may be attributed to the high quality of prepared nanocrystals with low amount of surface defects, as also demonstrated elsewhere [11].

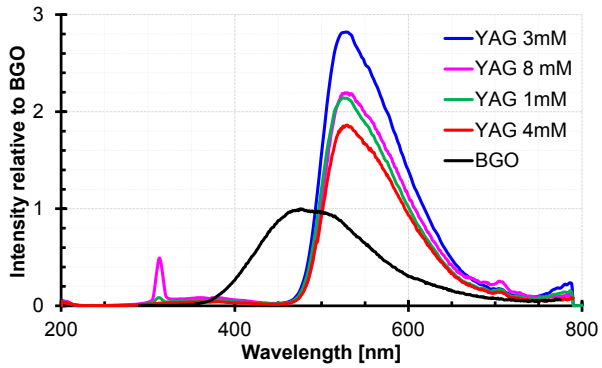

Figure 6 – Radioluminescence spectra of prepared garnet materials calcined at 1200 °C / 2 h and compared to the $Bi_4Ge_3O_{12}$ reference material (BGO).

3.3 Manufacturing cost evaluation

In order to estimate the manufacturing costs of the material and quantify the influence of production parameters on them, several contributions had to be assessed – capital costs (depreciation) φ, raw materials used χ, energy needed for the production and subsequent heat treatment of the product $\varepsilon+\tau$, and labour costs

λ. A detailed description of each contribution is provided within the Supplementary Information file, allowing modifications to the cost estimations under different conditions. In all cases, the costs were normalized to the mass of the material produced in a batch process [€/g] with properties / assumptions as close as possible to the photochemical production in the pilot plant discussed. Thus, the experimental synthesis yield represents a vital parameter strongly influencing the costs.

The *capital costs* were represented as equipment depreciation over a 5-year interval, assuming 49 weeks of operation a year and 104 hours per week for the pilot plant constituents, while 120 hours per week was assumed for heat treatment in a furnace. The *raw materials costs*, including type II purified water production costs, were calculated for chemicals with ~ 4N trace metal purity (99.99 %) available at a single supplier at the highest available batch size, while for raw materials without nominal metal ions or where the stated purity was based on chemical identity, the "per analysis" chemical grade was used. The *energy costs* calculations included the power consumption needed for both the photochemical process, and the subsequent heat treatment of products; a series of assumptions based on parameters of an arbitrarily chosen model furnace were used for the latter part. The *labour costs* were split into the actual synthesis of materials (including partial human overview during the process, 5 % of the synthesis time) and the subsequent separation of the product from the irradiated solutions. The former contribution, due to the essentially fixed time requirements for setting up the synthesis and draining the solutions afterward, causes the synthesis labour costs [€/g] to decrease sharply with the amount of material produced in a single production run. The latter contribution reflects mainly the morphology of the product – particulate solids are much easily filtered (thus, the associated labour costs are lower) than gelatinous products. The manufacturing costs are summarized in Table 2 for several different boundary conditions, including experimental parameters.

Table 2 – Estimated total manufacturing costs $\varphi + \chi + \varepsilon + \tau + \lambda$ [€/g] (VAT excluded) of various investigated materials in the photochemical pilot plant assuming several different boundary conditions: real experiments, theoretical limits for 100 % synthesis yield and both variants with industrial-scale filtering unit used.

Compound	Solution composition	Estimated manufacturing costs [€/g*]			
		Experiments	Limit	Experiments, industrial filtr.	Limit, industrial filtr.
$Y_3Al_5O_{12}$ (YAG)	2 mM YAG	9.30	9.11	2.99	2.90
	4 mM YAG	2.86	2.71	2.31	2.22
$Gd_3Ga_2Al_3O_{12}$	2 mM GGAG	10.41	10.14	4.13	3.93

(GGAG)	4 mM GGAG	4.16	3.91	3.62	3.42
$Zn_5(OH)_6(CO_3)_2$	10 mM Zn^{2+}, 0.2 M H_2O_2	8.30	4.10	5.76	3.61
	50 mM Zn^{2+}, 0.5 M H_2O_2	2.41	2.17	1.85	1.68
ZnO_2	20 mM Zn^{2+}, 1 M H_2O_2	16.18	5.22	13.25	4.73
	50 mM Zn^{2+}, 1 M H_2O_2	6.92	2.80	5.61	2.31

* mass of the final product (garnet or ZnO)

It can be readily seen from Fig. 7ac that due to the observed linearity in irradiation time versus garnet solution concentration (see Fig. 4), most costs per product weight are essentially constant for syntheses of a given garnet composition. The main differences lie in lower labour costs for higher garnet concentrations, reflecting both the ease of filtration and the lower contribution of the fixed time requirements.

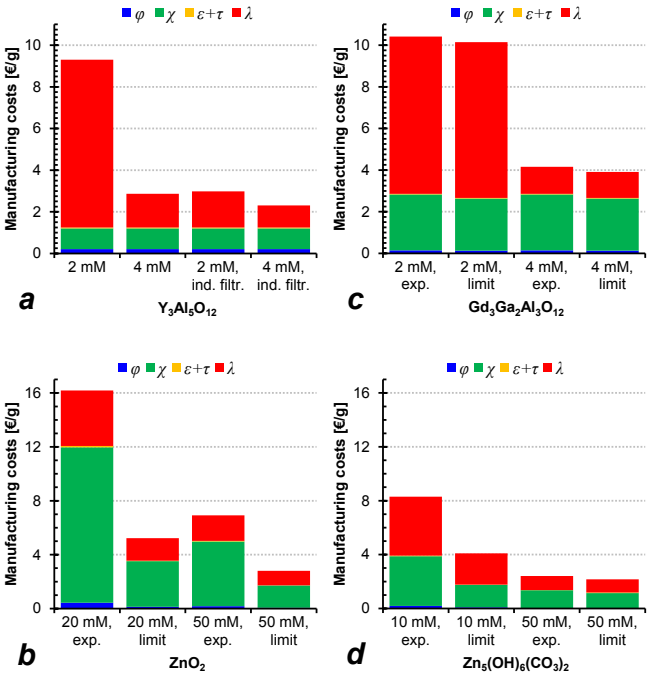

Figure 7 – Breakdown of manufacturing costs for various materials, comparing experimental values (observed synthesis yield) with theoretical limits (for 100 % yield) and the effect of using industrial-scale filtration unit (*a*).

On the other hand, the ZnO precursors (ZnO_2 and hydrozincite) show higher variation with solution composition, even taking into account the incomplete synthesis yields (see Fig. 7c,d). The theoretical limits for 100% synthesis yields vary significantly, strongly suggesting that the up-scaling of this peroxide-assisted synthesis needs much more detailed examinations to leverage both the manufacturing costs and the character of the product required for the intended application (e.g. as precursor for ultrafast ZnO:Ga scintillator).

Among the various contributions to the manufacturing costs, the labour costs are often dominating, as they reflect a very difficult filtration of the gelatinous products. The change in approximate filtration speed from laboratory-scale filtering methods to the parameters of the industrial-scale microfiltration apparatus newly installed at Tesla V.T. Mikroel led to a vast lowering of this cost contribution in the estimated manufacturing costs (see Table 2, Fig. 7a). Another lowering of the labour costs would require more process automation (simultaneously increasing the capital costs and energy costs), especially using on-line filtration of the solutions and/or automatic loading of concentrated solutions to keep the process fully continuous. However, such considerations exceed the scope of this paper. The raw materials costs comprise almost the whole remainder of the manufacturing costs, the most important contributions being Ga_2O_3 (for GGAG) and H_2O_2 (for ZnO and hydrozincite). Obviously, this part of the manufacturing costs depends primarily on the supply and demand on the market; bulk purchases of the needed chemicals may significantly lower the χ value.

4 **Conclusions**

Facile production of two main groups of nanocrystalline materials in large quantities in the photochemical pilot plant, their properties, and their estimated manufacturing costs have been thoroughly described. The irradiation of formate-containing solutions for a sufficiently long time led to a quantitative precipitation of gelatinous amorphous solid precursors for garnets $Y_3Al_5O_{12}$ and $Gd_3Ga_2Al_3O_{12}$, with synthesis yields slightly decreased to ~ 90–95 % due to separation losses. The required irradiation time for full conversion was found to increase linearly with the concentration of the initial solutions, using identical solution volumes and UV power, proving that this system can be easily up-scaled. At higher concentrations, the morphology of the produced material changed to a fine particulate, enabling much faster and easiear product separation. In the preparation of nanocrystalline ZnO through its solid precursors using photo-induced precipitation of zinc formate and hydrogen peroxide solutions, large differences were found in the character of the product. At large H_2O_2 concentrations (1 mol dm^{-3}), nanocrystalline ZnO_2 was observed, while the lower H_2O_2 concentrations led to the formation of basic zinc carbonate $Zn_5(OH)_6(CO_3)_2$, regardless of the Zn^{2+} concentration. However, the synthesis yields of the most desirable ZnO_2 were much lower than the expected chemical yields from the previous small-scale laboratory experiments, predominantly due to sorption of the product on any available surface. In order to achieve a cost-efficient up-scaled synthesis, further research

DOI: 10.1039/D1RE00374G

into the conditions that both prevent sorption of the product and keep its desirable properties for ZnO:Ga is required.

The chemical and phase purity of all materials produced, as well as luminescence of Ce- garnets, were fully consistent with the expected properties from laboratory-scale photochemical synthesis. Manufacturing costs in the current setup were also comprehensively estimated and possibilities for improvement of the cost-effectivity of the synthesis were outlined, suggesting that higher concentrations of solutions or more efficient filtration process lead to a less expensive manufacture of those materials.

The photochemical preparation method was proven to be very efficient for the synthesis of various nanocrystalline materials that can be readily up-scaled to industrial levels. Due to a largely unmanned operation and high production yields of materials, it is a very efficient and prospective method for synthesis of nanomaterials.

5 Conflicts of interest

There are no conflicts to declare.

6 Acknowledgements

Financial support of the Ministry of Industry and Trade of the Czech Republic (grant number FV30139) and Ministry of Education, Youth and Sports of the Czech Republic (grant number CZ.02.1.01/0.0/0.0/16_019/0000778) is gratefully acknowledged.

This research has received funding from the European Union's Horizon 2020 research and innovation programme under grant agreement No. 899293 – SPARTE. This publication reflects only the authors' view. The European Union is not liable for any use that may be made of the information contained herein.

7 References

1 F. Cambier, in: *Scientific bases for the preparation of heterogeneous catalysts: Proceedings of the 9th international symposium,* eds. E.M. Gaigneaux, M. Devillers, D.E. De Vos, S. Hermans, P.A. Jacobs and J.A. Martens, P. Ruiz„ *Stud. Surf. Sci. Catal.,* 2006, **162**, Production of catalysts with an inductive

atmospheric plasma torch, 243–250. https://doi.org/10.1016/S0167-2991(06)80913-4.

2 S.Yu. Sokovnin, V.G. Il'ves and M.G. Zuev, in: *Engineering of nanobiomaterials: Applications of nanobiomaterials, Volume 2*, ed. A.M. Grumezescu, Elsevier, 2016, Chapter 2 – Production of complex metal oxide nanopowders using pulsed electron beam in low-pressure gas for biomaterials application, 29–75.

3 B.G. Rao, D. Mukherjee and B.M. Reddy, in: *Nanostructures for Novel Therapy: Synthesis, Characterization and Applications*, eds.: D. Ficai and A.M. Grumezescu, Elsevier, 2017, Chapter 1 – Novel approaches for preparation of nanoparticles, 1–36.

4 F. Chen, E.B. Ehlerding and W.B. Cai, Theranostic Nanoparticles, *J. Nucl. Med.*, 2014, **55**, 1919–1922. https://doi.org/10.2967/jnumed.114.146019.

5 N. Ahmed, H. Fessi and A. Elaissari, Theranostic applications of nanoparticles in cancer, *Drug. Discov. Today*, 2012, **17**, 928–934. https://doi.org/10.1016/j.drudis.2012.03.010.

6 Y.J. Zhu, Y.T. Qian, M.W. Zhang, Z.Y. Chen, D.F. Xu, L. Yang and G.E. Zhou, Preparation and characterization of nanocrystalline powders of cuprous oxide by using γ-radiation. *Mater. Res. Bull.*, 1994, **29**, 377–383. https://doi.org/10.1016/0025-5408(94)90070-1.

7 P. He, X. Shen and H. Gao, Size-controlled preparation of Cu_2O octahedron nanocrystals and studies on their optical absorption, *J. Colloid Interface Sci.*, 2005, **284**, 510–515. https://doi.org/10.1016/j.jcis.2004.10.060.

8 Y. Hu, J. Chen, X. Xue, T. Li and Y. Xie, Room-temperature irradiation route to synthesize a large-scale single-crystalline ZnO hexangular prism, *Inorg. Chem.*, 2005, **44**, 7280–7282. https://doi.org/10.1021/ic050909o.

9 M.C. Rath, Y. Sunitha, H.N. Ghosh, S.K. Sarkar and T. Mukherjee, Investigation of the dynamics of radiolytic formation of ZnO nanostructured materials by pulse radiolysis, *Radiat. Phys. Chem.*, 2009, **78**, 77–80. https://doi.org/10.1016/j.radphyschem.2008.09.011.

10 V. Čuba, T. Gbur, V. Múčka, M. Nikl, R. Kučerková, M. Pospíšil and I. Jakubec, Properties of ZnO nanocrystals prepared by radiation method, *Radiat. Phys. Chem.*, 2010, **79**, 27–32. https://doi.org/10.1016/j.radphyschem.2009.08.006.

DOI: 10.1039/D1RE00374G

11 V. Čuba, J. Indrei, V. Múčka, M. Nikl, A. Beitlerová, M. Pospíšil and I. Jakubec, Radiation induced synthesis of powder yttrium aluminium garnet, *Radiat. Phys. Chem.*, 2011, **80**, 957–962. https://doi.org/10.1016/j.radphyschem.2011.04.009.

12 J. Bárta, M. Pospíšil and V. Čuba, Indirect synthesis of Al_2O_3 via radiation- or photochemical formation of its hydrated precursors, *Mater. Res. Bull.*, 2014, **49**, 633–639. https://doi.org/10.1016/j.materresbull.2013.10.005.

13 L. Procházková, J. Bárta, V. Čuba, C. Ekberg, S. Tietze and I. Jakubec, Gamma-radiolytic preparation of multi-component oxides, *Radiat. Phys. Chem.*, 2016, **124**, 68–74. https://doi.org/10.1016/j.radphyschem.2015.11.006.

14 T. Pavelková, V. Vaněček, I. Jakubec and V. Čuba, E-beam and UV induced fabrication of CeO_2, Eu_2O_3 and their mixed oxides with UO_2, *Radiat. Phys. Chem.*, 2016, **124**, 252–257. https://doi.org/10.1016/j.radphyschem.2015.10.022.

15 V. Čuba, J. Bárta, V. Jarý and M. Nikl, in: *Radiation synthesis of materials and compounds*, eds.: B.I. Kharisov, O.V. Kharissova and U.O. Mendez, CRC Press, Boca Raton, USA, 2013, Radiation-induced synthesis of oxide compounds, 81–100.

16 J. Bárta, L. Procházková, V. Vaněček, M. Kuzár, M. Nikl and V. Čuba, Photochemical synthesis of nano- and micro-crystalline particles in aqueous solutions, *Appl. Surf. Sci.*, 2019, **479**, 506–511. https://doi.org/10.1016/j.apsusc.2019.02.087.

17 D.N. Nikogosyan, A.A. Oraevsky and V.I. Rupasov, Two-photon ionization and dissociation of liquid water by powerful laser UV radiation, *Chem. Phys.*, 1983, **77**, 131–143. https://doi.org/10.1016/0301-0104(83)85070-8.

18 K. Azrague, E. Bonnefille, V. Pradines, V. Pimienta, E. Oliveros, M.-T. Maurette and F. Benoit-Marquié, Hydrogen peroxide evolution during V-UV photolysis of water, *Photochem. Photobiol. Sci.*, 2005, **4**, 406–408. https://doi.org/10.1039/B500162E.

19 K. Tomanová, M. Přeček, V. Múčka, L. Vyšín, L. Juha and V. Čuba, At the crossroad of photochemistry and radiation chemistry: formation of hydroxyl radicals in diluted aqueous solutions exposed to ultraviolet radiation, *Phys. Chem. Chem. Phys.*, 2017, **19**, 29402–29408. https://doi.org/10.1039/c7cp05125e.

20 C. Petersen, J. Thøgersen, S.K. Jensen and S.R. Keiding, Investigation of the primary photodynamics of the aqueous formate anion, *J. Phys. Chem. A*, 2006, **110**, 3383–3387. https://doi.org/10.1021/jp055976i.

21 F.R. Sharpe and I.H.L. Omrod, Fast isomerisation of humulone by photo-reaction: Preparation of an HPLC standard, *J.Inst. Brew.*, 1991, **97**, 33–37. https://doi.org/10.1002/j.2050-0416.1991.tb01050.x.

22 K. Higashi, S. Hosoyama, A. Ohno, S. Masuko, B.Yang, E. Sterner, Z. Wang, R.J. Linhardt and T. Toida, Photochemical preparation of a novel low molecular weight heparin, *Carbohydr. Polym.*, 2012, **67**, 1737–1743. https://doi.org/10.1016/j.carbpol.2011.09.087.

23 J. Kasanen, M. Suvanto and T.T. Pakkanen, Self-cleaning, titanium dioxide based, multilayer coating fabricated on polymer and glass surfaces, *J. Appl. Polym. Sci.*, 2009, **111**, 2597–2606. https://doi.org/10.1002/app.29295.

24 B.D. Mankidy, B. Joseph and V.K. Gupta, Photo-conversion of CO_2 using titanium dioxide: enhancements by plasmonic and co-catalytic nanoparticles, *Nanotechnol.,* 2013, **24**, 405402. https://doi.org/10.1088/0957-4484/24/40/405402.

25 S.S. Tan, L. Zou and E. Hu, Photocatalytic reduction of carbon dioxide into gaseous hydrocarbon using TiO_2 pellets, *Catal. Today*, 2006, **115**, 269–273. https://doi.org/10.1016/j.cattod.2006.02.057.

26 J. Bárta, V. Čuba, M. Pospíšil, V. Jarý and M. Nikl, Radiation-induced preparation of pure and Ce doped lutetium aluminium garnet and its luminescent properties, *J. Mater. Chem.*, 2012, **22**, 16590–16597. https://doi.org/10.1039/c2jm32766j.

27 T. Gbur, V. Čuba, V. Múčka, M. Nikl, K. Kníže k, M. Pospíšil and I. Jakubec, Photochemical preparation of ZnO nanoparticles, *J. Nanopart. Res.*, 2011, **13**, 4529–4537. https://doi.org/10.1007/s11051-011-0407-y.

28 L. Procházková, T. Gbur, V. Čuba, V. Jarý and M. Nikl, Fabrication of highly efficient ZnO nanoscintillators, *Opt. Mater.*, 2015, **47**, 67–71. https://doi.org/10.1016/j.optmat.2015.07.001.

29 V. Čuba, T. Pavelková, J. Bárta, V. Jarý, M. Nikl and I. Jakubec, Photo- and radiation-induced preparation of Y_2O_3 and Y_2O_3:Ce(Eu) nanocrystals, *J. Nanopart. Res.*, 2012, **14**, 794. https://doi.org/10.1007/s11051-012-0794-8.

30 I. Trenque, G.C. Magnano, J. Bárta, F. Chaput, M.A. Bolzinger, I. Pitault, S. Briançon, K. Masenelli-Varlot, M. Bugnet, C. Dujardin, V. Čuba and D. Amans, Synthesis routes of CeO_2 nanoparticles

dedicated to organophosphorus degradation: a benchmark, *CrystEngComm*, 2020, **22**, 1725–1737. https://doi.org/10.1039/c9ce01898k.

View Article Online
DOI: 10.1039/D1RE00374G

31 M. Sun, W.C. Hao, C.Z. Wang and T.M. Wang, A simple and green approach for preparation of ZnO_2 and ZnO under sunlight irradiation, *Chem. Phys. Lett.*, 2007, **443**, 342–346. https://doi.org/10.1016/j.cplett.2007.06.098.

32 Y. Lü, W. Zhang, H. Liu, Y. Sang, H. Qin, J. Tan and L. Tong, Synthesis of nano-sized and highly sinterable Nd:YAG powders by the urea homogeneous precipitation method, *Powder Technol.*, 2012, **217**, 140–147. https://doi.org/10.1016/j.powtec.2011.10.020.

33 A. Potdevin, G. Chadeyron, D. Boyer and R. Mahiou, Sol-gel based YAG:Ce^{3+} powders for applications in LED devices. *Phys. Status Solidi C*, 2007, **4**, 65–69. https://doi.org/10.1002/pssc.200673550.

34 E.R. Kupp, S. Kochawattana, S.-H. Lee, S. Misture and G.L. Messing, Particle size effects on yttrium aluminum garnet (YAG) phase formation by solid-state reaction, *J. Mater. Res.*, 2014, **29**, 2303–2311. https://doi.org/10.1557/jmr.2014.224.

35 J. Li, A.E. Smith, P. Jiang, J.K. Stalick, A.W. Sleight and M.A. Subramanian, True composition and structure of hexagonal "$YAlO_3$", actually $Y_3Al_3O_8CO_3$, *Inorg. Chem.*, 2015, **54**, 837–844. https://doi.org/10.1021/ic502027k.